Phase transition lowering under shock compression: The case of lead

Charles M. Pépin,[1,2,*] Mikhail A. Kozhaev,[3,†] Matteo Levantino,[3] and Arnaud Sollier[1,2]
[1] *CEA, DAM, DIF, 91297 Arpajon, France*
[2] *Université Paris-Saclay, CEA, Laboratoire Matière en Conditions Extrêmes, 91680 Bruyères-le-Châtel, France*
[3] *European Synchrotron Radiation Facility, 71 Avenue des Martyrs, CS 40220, 38043 Grenoble, France*

(Received 6 June 2025; accepted 10 August 2026; published 10 September 2026)

We report time-resolved x-ray diffraction measurements of lead (Pb) subjected to laser-driven shock compression up to the melt on nanosecond timescales. Along its Hugoniot, Pb exhibits a sequence of structural transitions markedly different from those observed under static compression. The conventional fcc-to-hcp transition is suppressed. Instead, the stacking fault probability in the fcc phase increases with compression up to ∼20 GPa, and the high-pressure bcc phase appears at 27 GPa, i.e., ∼60 GPa below the static hcp-bcc boundary at the same temperature. At 45.4 (±2.1) GPa and a calculated temperature of 2695 K, partial melting is evidenced by diffuse scattering, in excellent agreement with previous diamond anvil cell (DAC) melting data. Our results demonstrate that the dynamical response of Pb involves a distinct solid-state pathway, likely associated with stacking faults probability increase. These findings highlight the need to revisit phase diagrams under shock compression, particularly when coupled with time-resolved *in situ* microscopic diagnostics.

DOI: 10.1103/6qmk-qs9l

Over the past decade, the coupling of dynamic high-pressure science with advanced x-ray diagnostics has enabled the investigation of material structure and properties under extreme strain rates at the microstructural scale [1,2]. This synergy has opened new avenues for exploring phase diagrams under dynamic compression, granting access to previously unreachable pressure-temperature regimes [3–5]. In several cases, it has also revealed significant deviations from equilibrium phase boundaries, such as the emergence of intermediate phases [6] or shifts in phase transition pressures [7].

Surprisingly, certain materials, such as Si, Bi, and Sn [8–10], have exhibited a lowering of the phase transition threshold under dynamic loading. Lead (Pb), a group 14 element and the lighter homolog of Bi, has likewise attracted attention in both theoretical and experimental studies under static and dynamic compression. Under ambient conditions, Pb crystallizes in a face-centered cubic (fcc) structure and is valued for its shock-absorbing properties, ease of alloying, and effective electromagnetic shielding, attributes that make it indispensable in a wide range of technological and scientific applications.

Under static compression at room temperature, Pb undergoes a martensitic transformation to a hexagonal close-packed (hcp) structure near 13 GPa [11], involving a small volume collapse of ∼1%. At higher pressures (∼109 GPa), a second transition from hcp to bcc occurs [12]. Both transformations are characterized by sluggish kinetics, pronounced hysteresis, and persistent two-phase coexistence, owing to small free-energy differences and significant activation barriers.

While Pb's melting line has been extensively studied under static compression, substantial discrepancies have been reported between static and shock compression results [13–15], with the melting pressure threshold on the Hugoniot ranging from as low as 22 GPa to as high as 124 GPa [16–18]. Furthermore, the structural evolution of lead along its Hugoniot remains poorly understood, as prior studies have relied predominantly on macroscopic diagnostics such as velocimetry, without direct structural probes.

In this article, the structural evolution of Pb along its Hugoniot has been determined using accurate picosecond time-resolved synchrotron x-ray diffraction (XRD). The hcp-Pb structure is never observed. Instead, an increasing probability of stacking faults (SFs) in low-pressure fcc phase is observed along the Hugoniot, followed by the appearance of a bcc-type phase at 27 GPa—approximately 60 GPa below the static bcc transition line inferred from diamond anvil cell studies. The onset of melting is then observed at 45.4 GPa and 2695 K.

Experiments were carried out at the ID09 beamline of the European Synchrotron Radiation Facility using a pump-probe setup for shock generation and phase-compression analysis via XRD [10]. Shock waves were driven by an EKSPLA ANL5k laser, delivering up to 5 J at 1064 nm in 6.3 ns (full width at half maximum) pulses, focused to a 250 μm top-hat spot. Time-resolved XRD measurements employed 15 keV x-ray pulses (100 ps duration, $\sim10^9$ photons per pulse), collected on a Rayonix MX170-HS detector situated 120 mm from the sample, providing an angular coverage of approximately 40°. Laser-x-ray delays between 10 and 30 ns captured the dynamic response, with zero delay defined at the onset

*Contact author: charles.pepin@cea.fr
†Present address: Fibercryst S.A.S., 31 rue Wilson, 69150 Décines-Charpieu, France.

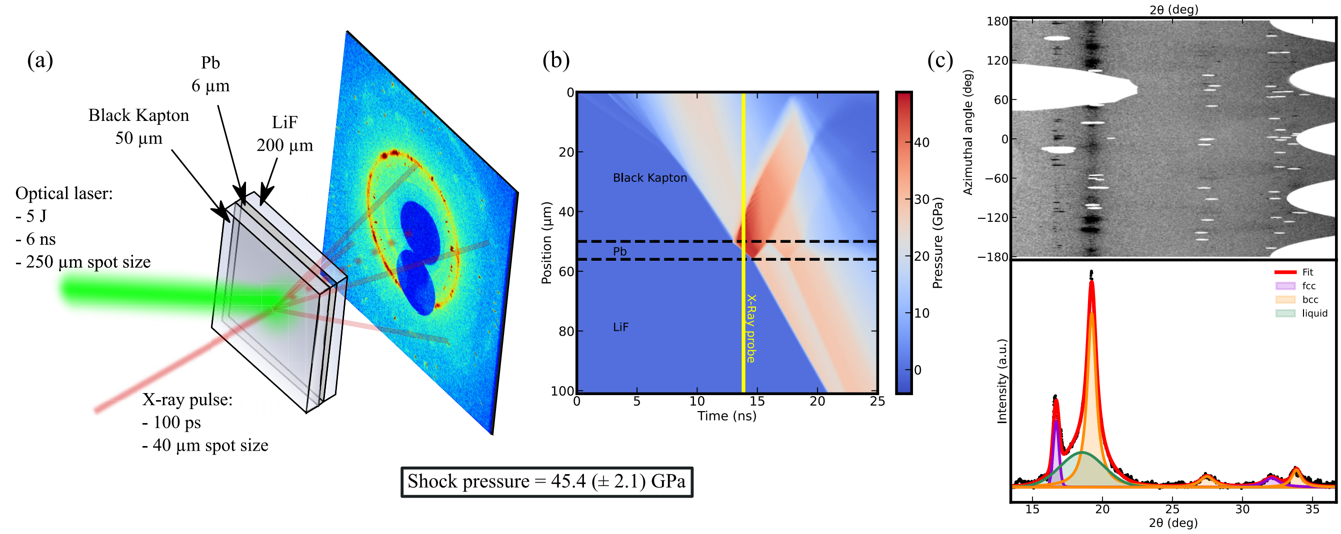

FIG. 1. Experimental setup. (a) The 15 keV ($\lambda = 0.8266$ Å), 100 ps x-ray pulse probes the shocked Pb samples and produces x-ray diffraction signal recorded on a Rayonix MX170-HS detector [10]. Raw diffraction dataset at a shock pressure of 45.4 (±2.1) GPa is presented, showing reflections from the high-pressure bcc phase and a broad diffuse scattering signal originating from dense liquid Pb. (b) Hydrodynamic simulation of the pressure distribution throughout the target package for the corresponding shot using the ESTHER code [19]. The horizontal dashed lines indicate material boundaries in Lagrangian coordinates and the yellow line is representative of the 100 ps x-ray probe at 14 ns. (c) Caked diffraction pattern corresponding to the same diffraction with the azimuthally integrated data below. The data are Le Bail fitted by an fcc phase (purple peaks) corresponding to uncompressed lead ahead of the shock, a bcc phase (orange peaks), and a liquid phase (green component).

of the laser rise. The target [Fig. 1(a)] consisted of a 50 µm Kapton ablator, a 6 µm 99.99% purity Pb foil ($\rho_0 = 11.346$ g/cm^3; Goodfellow), and a 200 µm LiF window, bonded with Angstrom Bond AB9110LV low-viscosity adhesive. Targets were mounted in vacuum (10^{-2} to 10^{-3} mbar) to mitigate atmospheric ionization. Laser energy tuning enabled control of peak shock pressures from 11 to 46 GPa, resulting in uniaxial compression of the Pb layer.

Velocity interferometer system for any reflector (VISAR) data could not be collected directly on the 6 µm Pb targets to complement our XRD findings. To address this issue, VISAR measurements were performed on thicker targets (Pb, 20 µm) and compared with hydrodynamic simulations from the ESTHER code [19]. The laser loading that effectively replicated these velocity signals was then utilized to simulate the thermodynamic conditions in the 6 µm Pb samples. SESAME [20] is used in the hydrodynamic simulations because the model of Dai *et al.* [21] describes the Hugoniot temperature rather than providing a complete tabulated EOS. The hydrodynamic simulations of the pressure-distance profiles through the 6 µm Pb sample confirm that the pressure state in the shocked bulk is nearly uniform at the time of the XRD probe, with gradients comparable to the experimental uncertainties (see Ref. [22]). The pump-probe delay was incrementally increased until the first x-ray diffraction peaks of the compressed sample emerged, thus confirming that measurements were taken along the Hugoniot.

Figure 1(a) shows the two-dimensioanl orthographic view of diffraction data for a shock pressure of 45.4 GPa (±2.1 GPa) and the corresponding hydrodynamic simulation in Fig. 1(b). At this pressure, we observe a weak signal from the uncompressed lead ahead of the shock [purple peaks in Fig. 1(c)], a compressed lead in the high-pressure bcc phase (orange peaks), and a broad diffuse scattering signal at 2θ values consistent with dense liquid lead. This diffuse scattering is uniform azimuthally and indicates partial melting onset at this pressure. X-ray diffraction of the remaining solid part allows us to determine the density of the compressed sample. Pressure can then be determined using the Rankine-Hugoniot relations:

$$\rho_0 u_s = \rho(u_s - u_p), \tag{1}$$

$$P - P_0 = \rho_0 u_s u_p, \tag{2}$$

and using the linear shock Hugoniot

$$u_s = c_0 + s u_p,$$

with ρ_0 the initial density, ρ the density behind the shock, u_s the shock speed, u_p the particle velocity behind the shock, P_0 (=0 at ambient pressure), and P the shock upstream and downstream pressures, respectively. Solving Eqs. (1) and (2) for P gives

$$P_H = \frac{\rho_0 c_0^2\, \varepsilon}{(1 - \varepsilon s)^2},$$

$$\varepsilon = 1 - \frac{V}{V_0} = 1 - \frac{\rho_0}{\rho}.$$

Using the values $c_0 = 2.05$ km/s, $s = 1.46$, and $\rho_0 = 11.346$ g/cm^3 from Ref. [21] gives the aforementioned pressure. The error bars arise from the fitting errors.

No direct temperature measurements were possible in this study; therefore, temperature estimates rely on calculated pressure-temperature Hugoniot paths. Three such paths are

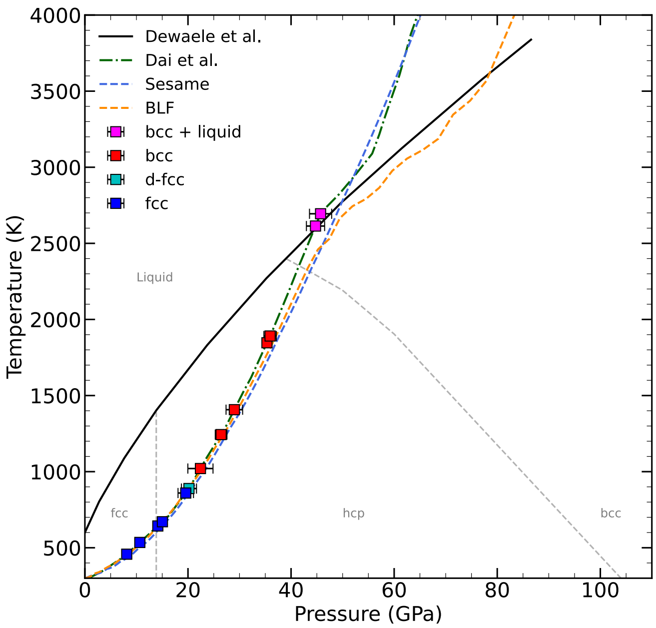

FIG. 2. Phase diagram of lead. Experimental phases determined in the present study (closed symbols) are overlaid on previously determined Hugoniot curves from Dai *et al.* [21] (green line), SESAME [20] (blue line), and BLF [23,24] (orange line). The graph also shows the melting line reported by Dewaele *et al.* [15] (black line), the fcc-hcp boundary determined by Kznetsov *et al.* [11], and the room-temperature hcp-bcc transition by Mao *et al.* [12] (dashed gray lines). The dashed gray line between the ambient-temperature bcc transition and its high-temperature extension was added for clarity and does not appear in the original datasets.

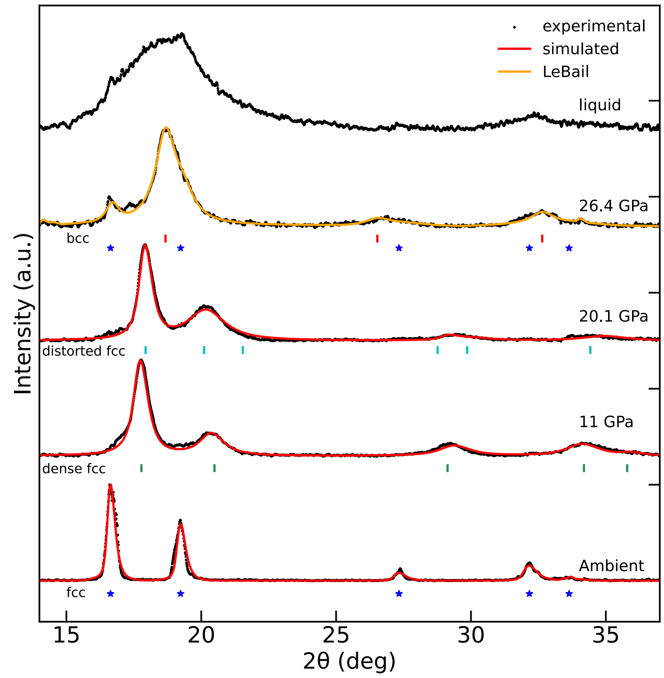

FIG. 3. X-ray diffraction. Azimuthally averaged diffraction data as a function of increasing shock pressure. The measured diffractograms are represented in black, the corresponding simulated profile in red, and the LeBail fit for the bcc phase in orange. A dense fcc phase is observed at 11 GPa, while at 20.1 GPa the data are best simulated by a distorted fcc. A typical diffractogram of the high-pressure bcc phase is shown at 26.4 GPa, i.e., 60 GPa below the static bcc transition line inferred from diamond-anvil-cell studies.

shown in Fig. 2. Using the shock Hugoniot of Dai *et al.* [21] to convert pressure into temperature yields a value of $T = 2695$ K, which is in excellent agreement with the melting line determined by laser heating of Pb in a diamond anvil cell [15]. The end of the melting plateau could not be identified, as neither VISAR nor XRD provides reliable pressure measurements in a fully molten sample. Nevertheless, a mere 5% increase in laser transmission (from 50% to 55%) was sufficient to induce complete melting, suggesting that the coexistence pressure interval is narrow. Moreover, Ref. [25] suggested that Pb is fully liquid at 54.5 GPa based on sound velocity measurements, consistent with our findings. These observations support the use of the Hugoniot proposed by Dai *et al.* [21] over alternative models (Sesame [20], BLF [23,24]) for shock-compressed Pb.

To track structural changes under shock compression, such as stacking fault formation or phase transitions, the experimental x-ray diffraction line profiles are quantitatively compared with forward simulations. The simulated profiles take into account all key experimental parameters, such as the sample thickness, the sample-detector distance, the quasi-monochromatic spectral flux from the ID09 beamline, and the instrumental broadening. These quantities are incorporated into the Warren-Velterop formalism that quantitatively simulates the effects of the SFs on the diffraction line profile in an fcc material [26,27] and which was successfully employed in other XRD experiments of shock-compressed noble metals [28–30]. In this description, the increasing SF probability shifts the (200) peak toward the (111). To reproduce the observed peak widths, the simulations are convoluted with a Lorentzian broadening function, which increases with shock stress. During the fitting process, the relative intensities of the simulated hkl reflections are adjusted to capture the textured nature of the lead foils. Details of the forward-simulation approach are presented in Ref. [22].

By reducing the laser transmission to as low as 5%, the solid Hugoniot was probed down to 8.1 GPa and a calculated temperature of 458 K, where compressed fcc-Pb is unambiguously identified (Fig. 3). Under quasistatic compression, fcc-Pb transforms to an hcp phase above 14 GPa, with the transition pressure remaining constant up to the melting curve [11]. In contrast, shock loading never produces hcp-Pb; instead, the low-pressure fcc lattice develops an increasing SF probability with compression, leading to a pronounced tetragonal distortion at 20.1 GPa. Figure 3 shows the evolution of the diffraction line profiles as a function of shock pressure, along with the simulated XRD profiles taking into account the stacking faults in the fcc phase (red lines). The fcc phase is observed up to 20.1 GPa, with the SF probability increasing up to ∼12% at 20.1 GPa, as shown in Fig. 4. The dependence of SF probability with volume compression mirrors trends observed in molecular-dynamics simulations [31] and experimentally [28–30].

At 20.1 GPa, the XRD simulation including SFs could not successfully match the observed diffraction profile [22].

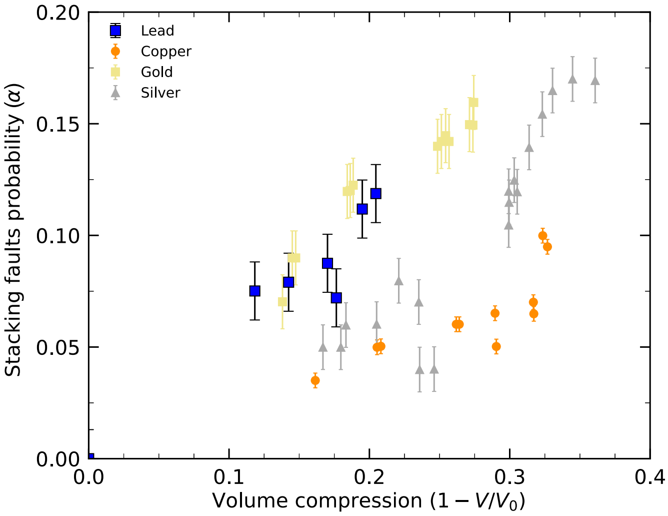

FIG. 4. Stacking fault probability vs volume compression for the present study (Pb, blue squares) compared to previous results for Au [30] (yellow squares), Ag [29] (gray triangles), and Cu [28] (orange points).

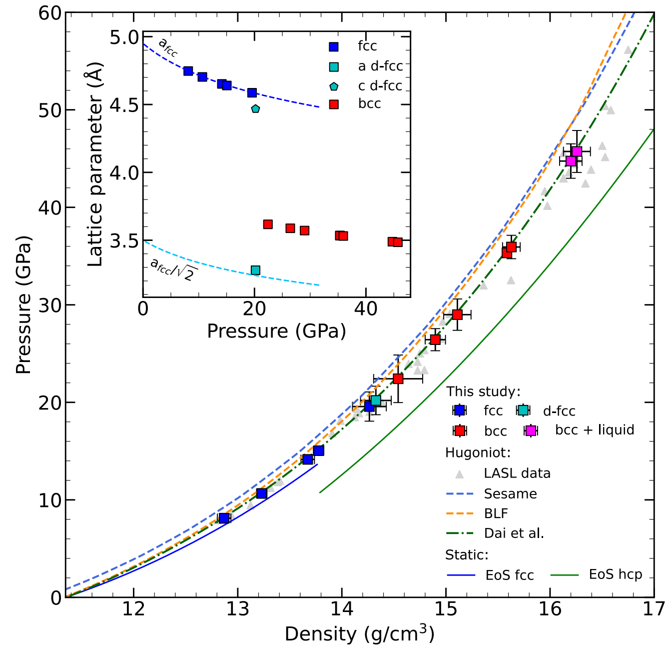

FIG. 5. Pressure vs density plot. P-ρ experimental points from this study for each phase (squares, blue: fcc, cyan: distorted fcc, red: bcc, magenta: bcc-liquid coexistence) alongside previously published Hugoniot data [32] (gray triangles) and 300 K static equation of state (EoS) [34,41] (blue and green curves). Three Hugoniot models are also shown (dashed curves): Dai *et al.* [21], BLF [23,24], and SESAME [20]. Inset: Evolution of the measured lattice parameters as a function of pressure. The calculated evolutions of both the fcc lattice parameter a_{fcc} and its value normalized by $\sqrt{2}$ are shown as dashed lines.

A tetragonal distortion was introduced to better match the observed profile. The tetragonal distortion splits both the [200] and [220] reflections, reproducing the measured peak positions. Moreover, the measured density of the distorted-fcc phase matches the continuum Hugoniot data [32] (Fig. 5), confirming its thermodynamic plausibility under shock loading.

Upon further compression, a bcc-type phase emerges at 27 GPa, approximately 60 GPa below the static bcc transition line inferred from diamond-anvil-cell studies at the same temperature [15,33,34]. A similar early onset of bcc-Pb was noted but overlooked in a prior dynamic experiment [35]. The fcc → bcc transformation is consistent with the classical Bain mechanism, a diffusionless, martensitic pathway achieved by uniaxial contraction along one cubic axis and simultaneous expansion along the orthogonal axes. This distortion preserves atomic connectivity, enabling rapid rearrangement under shock-loading conditions. The evolution of lattice parameters measured here (Fig. 5, inset) closely follows the Bain-predicted trajectory shown as dashed curves. Several orientation relationships (ORs), including the Bain distortion itself, the Kurdjumov-Sachs-Nishiyama shear model, the Bogers-Burgers mechanism, and the one-step Pitsch distortion, have been proposed for martensitic transformations [36–39]. Recent shock-compression experiments on other materials have successfully discriminated among these ORs [6,40]. In our case, however, the highly textured Pb samples [Fig. 1(a)] transform into a fine powder in the bcc phase and prevent unambiguous OR determination.

By measuring the longitudinal and transverse stress components in lead under shock compression, Bat'kov *et al.* observed a decrease in the dynamic yield strength around 22 GPa [17], while Carter determined a minor change of slope in the U_s–U_p curve above 27.5 GPa [18]. These features were initially attributed to shock-induced melting; however, advances in the understanding of the phase diagram [15] together with the present study now allow this hypothesis to be ruled out. Notably, these pressures coincide with the fcc → bcc transition domain identified in this work, which could explain these observations. While these earlier macroscopic observations pointed to an anomaly in this pressure range, they lacked the structural identification necessary to distinguish between melting and a solid-state phase transition. The present XRD data resolve this ambiguity.

Recent shock-compression experiments by Krygier *et al.* [42] have demonstrated that lead, ordinarily one of the softest metals at ambient conditions, can attain flow stresses of nearly 4 GPa when subjected to nanosecond-scale shocks. By integrating time-resolved x-ray radiography with fits to the improved Steinberg-Guinan strength model [43], they attributed this dramatic hardening to a diffusionless fcc → bcc transformation. The modeling suggested the onset of the bcc phase at low pressures, but the transformation itself remained indirectly inferred and lacked direct structural confirmation. The present work provides the first clear crystallographic evidence of this fcc-to-bcc transformation in dynamically compressed Pb, firmly establishing the structural origin of the anomalous hardening behavior. Furthermore, our results indicate that the bcc phase appears at significantly lower pressures than previously thought, suggesting that the hardening mechanism may become active earlier along the compression pathway.

This study provides direct evidence for a shock-induced fcc-bcc phase transition in Pb, extending the findings previously reported for the noble metals Au, Cu, and Ag

[3,4,28–30]. The recurrence of this transformation across fcc metals points to a shared mechanism, whose key ingredient is the generation of SFs: Under shock loading, the SF probability rises to 10%–15% (Fig. 4), producing disordered structures that stabilize the bcc phase by lowering its Gibbs free energy relative to fcc, in line with theoretical predictions [44]. Our Pb data follow the same trend, both in the magnitude of the measured SF probability and in the resulting lowering of the transition pressure, consistent with the low Stacking Faults Energy (SFE) of lead [45,46]. Within the fcc metals, Ni stands out as an exception: Despite a relatively low SFE [46], it shows no shock-induced fcc-bcc transition, suggesting that a threshold may exist above which SFs are insufficient to trigger the transformation. Establishing a quantitative link between SFE and transition pressure is an interesting direction for future investigation.

Whether planar-fault energetics play a comparable role beyond the close-packed metals is an open question, but we note that transition lowering under dynamic loading has also been reported for Si [8], Sb [47], Bi [9], and TiO_2 [48]. Si possesses a very low SFE [49], comparable to that of Ag. Sb and Bi crystallize in the rhombohedral A7 structure, which is not close-packed, so that a generalized stacking-fault energy surface (γ surface) would have to be considered instead of the standard SFE. No such data are available for the elemental forms, nor for TiO_2. We therefore offer this only as a hypothesis worth testing, and one that would require dedicated γ-surface calculations on these systems.

In conclusion, our nanosecond time-resolved x-ray diffraction measurements reveal that, under laser-driven shock loading, lead follows a crystallographic pathway fundamentally distinct from its static counterpart. Instead of the low-pressure fcc → hcp transition, we observe the fcc phase at low pressures, accommodating an increasing probability of SFs, up to 12%, followed by the appearance of the known bcc phase at ∼27 GPa, approximately 60 GPa below its static stability domain. This lowering of the phase-transition threshold appears to be driven by the generation of SFs and to be a common trait of materials with low SFE. Finally, the onset of partial melting evidenced by diffuse scattering at 45.4 (±2.1) GPa and for a calculated temperature of 2695 K is in excellent agreement with the diamond-anvil cell-determined melting line, resolving discrepancies between shock and static measurements. These findings underscore the importance of time-resolved diagnostics in deciphering the complex pathways of structural transformations under extreme dynamic loading.

ACKNOWLEDGMENT

The authors acknowledge the European Synchrotron Radiation Facility for provision of synchrotron radiation facilities on beamline ID09, during beam time allocated to the long-term proposal HC-4528.

DATA AVAILABILITY

The data that support the findings of this article are openly available at Ref. [50], embargo periods may apply.

[1] S. Pascarelli, M. McMahon, C. Pépin, O. Mathon, R. F. Smith, W. L. Mao, H.-P. Liermann, and P. Loubeyre, Materials under extreme conditions using large x-ray facilities, Nat. Rev. Methods Primers **3**, 82 (2023).

[2] J. S. Wark, M. I. McMahon, and J. H. Eggert, Femtosecond diffraction and dynamic high pressure science, J. Appl. Phys. **132**, 080902 (2022).

[3] S. M. Sharma, S. J. Turneaure, J. M. Winey, Y. Li, P. Rigg, A. Schuman, N. Sinclair, Y. Toyoda, X. Wang, N. Weir, J. Zhang, and Y. M. Gupta, Structural transformation and melting in gold shock compressed to 355 GPa, Phys. Rev. Lett. **123**, 045702 (2019).

[4] R. Briggs, F. Coppari, M. G. Gorman, R. F. Smith, S. J. Tracy, A. L. Coleman, A. Fernandez-Pañella, M. Millot, J. H. Eggert, and D. E. Fratanduono, Measurement of body-centered cubic gold and melting under shock compression, Phys. Rev. Lett. **123**, 045701 (2019).

[5] M. G. Gorman, S. Elatresh, A. Lazicki, J. R. Rygg, J. H. Eggert, S. Hamel, A. F. Goncharov, L. R. Benedetti, and J. M. McMahon, Experimental observation of open structures in elemental magnesium at terapascal pressures, Nat. Phys. **18**, 1307 (2022).

[6] S. Singh, M. G. Gorman, P. G. Heighway, J. V. Bernier, D. McGonegle, H. J. Lee, B. Nagler, J. H. Eggert, and R. F. Smith, Unexpected observation of disorder and multiple phase-transition pathways in shock-compressed Zr, Phys. Rev. Lett. **133**, 096101 (2024).

[7] R. Briggs, M. G. Gorman, A. L. Coleman, R. S. McWilliams, E. E. McBride, D. McGonegle, J. S. Wark, L. Peacock, S. Rothman, S. G. Macleod, *et al.*, Ultrafast x-ray diffraction studies of the phase transitions and equation of state of scandium shock compressed to 82 GPa, Phys. Rev. Lett. **118**, 025501 (2017).

[8] E. E. McBride, A. Krygier, A. Ehnes, E. Galtier, M. Harmand, Z. Konôpková, H. J. Lee, H.-P. Liermann, B. Nagler, A. Pelka, M. Rödel, A. Schropp, R. F. Smith, C. Spindloe, D. C. Swift, F. Tavella, S. Toleikis, T. Tschentscher, J. S. Wark, and A. Higginbotham, Phase transition lowering in dynamically compressed silicon, Nat. Phys. **15**, 89 (2019).

[9] C. M. Pépin, A. Sollier, A. Marizy, F. Occelli, M. Sander, R. Torchio, and P. Loubeyre, Kinetics and structural changes in dynamically compressed bismuth, Phys. Rev. B **100**, 060101(R) (2019).

[10] A. Sollier, C. Pépin, M. Kozhaev, C. Mariette, W. Reichenbach, and M. Levantino, Development of a laser-driven shock compression platform for time-resolved XRD experiments at the ID09 beamline of the European Synchrotron Radiation Facility, High Press. Res. **44**, 418 (2024).

[11] A. Kuznetsov, V. Dmitriev, L. Dubrovinsky, V. Prakapenka, and H. P. Weber, FCC–HCP phase boundary in lead, Solid State Commun. **122**, 125 (2002).

[12] H. K. Mao, Y. Wu, J. F. Shu, J. Z. Hu, R. J. Hemley, and D. E. Cox, High-pressure phase transition and equation of state of lead to 238 GPa, Solid State Commun. **74**, 1027 (1990).

[13] B. K. Godwal, C. Meade, R. Jeanloz, A. Garcia, A. Y. Liu, and M. L. Cohen, Ultrahigh-pressure melting of lead: A multidisciplinary study, Science **248**, 462 (1990).

[14] D. Partouche-Sebban, J. L. Pélissier, F. G. Abeyta, W. W. Anderson, M. E. Byers, D. Dennis-Koller, J. S. Esparza, R. S. Hixson, D. B. Holtkamp, B. J. Jensen, J. C. King, P. A. Rigg, P. Rodriguez, D. L. Shampine, J. B. Stone, D. T. Westley, S. D. Borror, and C. A. Kruschwitz, Measurement of the shock-heated melt curve of lead using pyrometry and reflectometry, J. Appl. Phys. **97**, 043521 (2005).

[15] A. Dewaele, M. Mezouar, N. Guignot, and P. Loubeyre, Melting of lead under high pressure studied using second-scale time-resolved x-ray diffraction, Phys. Rev. B **76**, 144106 (2007).

[16] G. E. Duvall and R. A. Graham, Phase transitions under shock-wave loading, Rev. Mod. Phys. **49**, 523 (1977).

[17] Yu. V. Bat'kov, V. N. German, R. S. Osipov, S. A. Novikov, and V. A. Tsyganov, Melting of lead in shock compression, J. Appl. Mech. Tech. Phys. **29**, 139 (1988).

[18] W. J. Carter, Metallurgical effects at high strain rates, in *Metallurgical Effects at High Strain Rates*, edited by R. W. Rohde, B. M. Butcher, J. R. Holland, and C. H. Karnes (Plenum Press, New York, 1973), p. 171.

[19] J. P. Colombier, P. Combis, F. Bonneau, R. Le Harzic, and E. Audouard, Hydrodynamic simulations of metal ablation by femtosecond laser irradiation, Phys. Rev. B **71**, 165406 (2005).

[20] J. Johnson and S. Lyon, SESAME: The Los Alamos National Laboratory Equation of State Database, Technical Report LA-UR 92-3407, Los Alamos National Laboratory (1992), https://cdn.lanl.gov/files/laur-92-3407_a0e99.pdf.

[21] C. Dai, H. Tan, and H. Geng, Model for assessing the melting on Hugoniots of metals: Al, Pb, Cu, Mo, Fe, and U, J. Appl. Phys. **92**, 5019 (2002).

[22] See Supplemental Material at http://link.aps.org/supplemental/10.1103/6qmk-qs9l for additional experimental data and simulation details.

[23] A. V. Bushman and V. E. Fortov, Model equations of state, Sov. Phys. Usp. **26**, 465 (1983).

[24] I. V. Lomonosov, A. V. Bushman, and V. E. Fortov, Equations of state for metals at high energy densities, AIP Conf. Proc. **309**, 117 (1994).

[25] D. A. Boness, J. M. Brown, and J. W. Shaner, Shock waves in condensed matter, in *Shock Waves in Condensed Matter*, edited by S. C. Schmidt and N. C. Holmes (Elsevier, New York, 1988), p. 115.

[26] B. E. Warren, *X-ray Diffraction* (Addison-Wesley, Reading, MA, 1969).

[27] L. Velterop, R. Delhez, T. H. de Keijser, E. J. Mittemeijer, and D. Reefman, X-ray diffraction analysis of stacking and twin faults in f.c.c. metals: A revision and allowance for texture and non-uniform fault probabilities, J. Appl. Cryst. **33**, 296 (2000).

[28] S. M. Sharma, S. J. Turneaure, J. M. Winey, and Y. M. Gupta, Transformation of shock-compressed copper to the body-centered-cubic structure at 180 GPa, Phys. Rev. B **102**, 020103 (2020).

[29] S. M. Sharma, S. J. Turneaure, J. M. Winey, and Y. M. Gupta, What determines the fcc-bcc structural transformation in shock compressed noble metals? Phys. Rev. Lett. **124**, 235701 (2020).

[30] S. M. Sharma, S. J. Turneaure, J. M. Winey, P. A. Rigg, N. Sinclair, X. Wang, Y. Toyoda, and Y. M. Gupta, Real-time observation of stacking faults in gold shock compressed to 150 GPa, Phys. Rev. X **10**, 011010 (2020).

[31] B. L. Holian and P. S. Lomdahl, Plasticity induced by shock waves in nonequilibrium molecular-dynamics simulations, Science **280**, 2085 (1998).

[32] S. P. Marsh, *LASL Shock Hugoniot Data* (University of California Press, Berkeley, 1980).

[33] S. Anzellini, A. K. Kleppe, D. Daisenberger, M. T. Wharmby, R. Giampaoli, S. Boccato, M. A. Baron, F. Miozzi, D. S. Keeble, A. Ross, S. Gurney, J. Thompson, G. Knap, M. Booth, L. Hudson, D. Hawkins, M. J. Walter, and H. Wilhelm, Laser-heating system for high-pressure X-ray diffraction at the Extreme Conditions beamline I15 at Diamond Light Source, J. Synchrotron Radiat. **25**, 1860 (2018).

[34] A. Dewaele, Equations of state of simple solids (including Pb, NaCl and LiF) compressed in helium or neon in the Mbar range, Minerals **9**, 684 (2019).

[35] D. McGonegle, P. G. Heighway, M. Sliwa, C. A. Bolme, A. J. Comley, L. E. Dresselhaus-Marais, A. Higginbotham, A. J. Poole, E. E. McBride, B. Nagler, I. Nam, M. H. Seaberg, B. A. Remington, R. E. Rudd, C. E. Wehrenberg, and J. S. Wark, Investigating off-Hugoniot states using multi-layer ring-up targets, Sci. Rep. **10**, 13172 (2020).

[36] E. C. Bain and N. Dunkirk, The nature of martensite, AIME Trans. **70**, 25 (1924).

[37] Z. Nishiyama, Martensitic transformation, in *Martensitic Transformation*, edited by M. E. Fine, M. Meshii, and C. M. Wayman (Academic Press, New York, 1978), pp. 344–411.

[38] A. J. Bogers and W. G. Burgers, Partial dislocations on the 110 planes in the b.c.c. lattice and the transition of the f.c.c. into the b.c.c. lattice, Acta Metall. **12**, 255 (1964).

[39] C. Cayron, One-step model of the face-centred-cubic to body-centred-cubic martensitic transformation, Acta Cryst. A **69**, 498 (2013).

[40] M. Sims, R. Briggs, T. J. Volz, S. Singh, S. Hamel, A. L. Coleman, F. Coppari, D. J. Erskine, M. G. Gorman, B. Sadigh, J. Belof, J. H. Eggert, R. F. Smith, and J. K. Wicks, Experimental and theoretical examination of shock-compressed copper through the fcc to bcc to melt phase transitions, J. Appl. Phys. **132**, 075902 (2022).

[41] Th. Strässle, S. Klotz, K. Kunc, V. Pomjakushin, and J. S. White, Equation of state of lead from high-pressure neutron diffraction up to 8.9 GPa and its implication for the NaCl pressure scale, Phys. Rev. B **90**, 014101 (2014).

[42] A. Krygier, P. D. Powell, J. M. McNaney, C. M. Huntington, S. T. Prisbrey, B. A. Remington, R. E. Rudd, D. C. Swift, C. E. Wehrenberg, A. Arsenlis, H.-S. Park, P. Graham, E. Gumbrell, M. P. Hill, A. J. Comley, and S. D. Rothman, Extreme hardening of Pb at high pressure and strain rate, Phys. Rev. Lett. **123**, 205701 (2019).

[43] R. E. Rudd, L. H. Yang, P. D. Powell, P. Graham, A. Arsenlis, R. M. Cavallo, A. G. Krygier, J. M. McNaney, S. T. Prisbrey, B. A. Remington, D. C. Swift, C. E. Wehrenberg, and H.-S. Park, Modeling laser-driven high-rate plasticity in BCC lead, AIP Conf. Proc. **1979**, 070027 (2018).

[44] W. Ling, B. Chen, Q. Zeng, X. Yu, S. Zhang, Z. Zhao, and J. Dai, Atomic insight into phase transition lowering in shock compressed copper, Front. Phys. **10**, 838316 (2022).

[45] G. Bolling, L. Hays, and H. Wiedersich, The plasticity of lead single crystals and the determination of stack-fault energy, Acta Metall. **10**, 185 (1962).

[46] N. M. Rosengaard and H. L. Skriver, Calculated stacking-fault energies of elemental metals, Phys. Rev. B **47**, 12865 (1993).

[47] A. L. Coleman, M. G. Gorman, R. Briggs, R. S. McWilliams, D. McGonegle, C. A. Bolme, A. E. Gleason, D. E. Fratanduono, R. F. Smith, E. Galtier, H. J. Lee, B. Nagler, E. Granados, G. W. Collins, J. H. Eggert, J. S. Wark, and M. I. McMahon, Identification of phase transitions and metastability in dynamically compressed antimony using ultrafast x-ray diffraction, Phys. Rev. Lett. **122**, 255704 (2019).

[48] I. K. Ocampo, R. F. Smith, D. Kim, V. Prakapenka, S. Speziale, M. Schoelmerich, K. Appel, D. N. Polsin, M. Marshall, S. J. Tracy, F. Miozzi, H. J. Lee, E. Galtier, E. Cunningham, C. McGuire, C. Vennari, A. E. Gleason, and T. S. Duffy, Ultrafast x-ray diffraction of high-pressure phases in dynamically compressed TiO_2, Phys. Rev. B **112**, 104103 (2025).

[49] M. Y. Chou, M. L. Cohen, and S. G. Louie, Theoretical study of stacking faults in silicon, Phys. Rev. B **32**, 7979 (1985).

[50] 10.15151/ESRF-ES-1710755704